Numerical simulation of the zebra pattern formation on a three-dimensional model

Darae Jeong [a], Yibao Li [b], Yongho Choi [a], Minhyun Yoo [a], Dooyoung Kang [c], Junyoung Park [c], Jaewon Choi [c], Junseok Kim [a],*

[a] *Department of Mathematics, Korea University, Seoul 02841, Republic of Korea*
[b] *School of Mathematics and Statistics, Xi'an Jiaotong University, Xi'an 710049, China*
[c] *Seoul Science High School, Seoul 03066, Republic of Korea*

HIGHLIGHTS

- We numerically investigate the zebra skin pattern formation on a zebra model.
- We use Lengyel–Epstein model: a two component activator and inhibitor system.
- We provide computational experiments to study the pattern formation.

ARTICLE INFO

ABSTRACT

In this paper, we numerically investigate the zebra skin pattern formation on the surface of a zebra model in three-dimensional space. To model the pattern formation, we use the Lengyel–Epstein model which is a two component activator and inhibitor system. The concentration profiles of the Lengyel–Epstein model are obtained by solving the corresponding reaction–diffusion equation numerically using a finite difference method. We represent the zebra surface implicitly as the zero level set of a signed distance function and then solve the resulting system on a discrete narrow band domain containing the zebra skin. The values at boundary are dealt with an interpolation using the closet point method. We present the numerical method in detail and investigate the effect of the model parameters on the pattern formation on the surface of the zebra model.

1. Introduction

Although the pattern in living organisms is one of the classical problems of morphogenesis which explains how animals such as mammals, seashells, and marine fishes and vegetation evolve differently resulting in a consolidated and stable pattern [1–3], it had been generally believed that how the skin pattern in living organisms, especially mammals, is generated genetically is unclear. Nevertheless, pattern formation based on the Turing model has been one of the notable exceptions since the middle part of the 20th century while acceptance in bioinformatics of mathematical biology has been slower [4]. Most mathematical models of these patterns are based on a reaction–diffusion model, which was first proposed by Turing [5]. The reaction–diffusion model, the system of two distributed reacting and diffusing chemicals, could generate spatial

---

Fig. 1. (a) Schematic illustration of the surface S, the narrow band domain Ω_δ with thickness 2δ, and its boundary $\partial\Omega_\delta$. (b) Closest points $\text{cp}(\mathbf{x}_1)$ and $\text{cp}(\mathbf{x}_2)$ for points $\mathbf{x}_1, \mathbf{x}_2 \in \partial\Omega_\delta$.

patterns autonomously. Murray [6] presented the reaction–diffusion mechanism for laying down of the pre-patterns for animal marking. Young [7] performed the simulation that cells lay out on a grid with an activator and an inhibitor. Barrio et al. [8] studied numerically the spatial pattern formation with the Turing's model on the two-dimensional domain. Also, activator–inhibitor systems with non-local coupling are studied in two dimensions by Silva et al. [9]. Painter et al. [10] proposed the robustly generated patterns without parameter control which is overcome that the difficulty of applicability of classical Turing models to pattern formation is limited by the sensitivity of patterns to model parameters. Based on Turing's hypothesis, evolving morphogenetic fields in the zebra skin pattern was researched by Grávan and Lahoz-Beltra [1]. Guiu-Souto et al. [11] introduced a set of quantitative morphological measures that describe the geometrical and topological properties of Turing patterns (area, boundary length, cluster numbering, connectivity, and so on) for easily distinguish among different Turing structures.

The theoretically predicted patterns has been demonstrated under controlled experimental conditions in a Chlorite–Iodide–Malonic Acid–Starch (CIMA) reaction [12–14]. Lengyel and Epstein [15–17] derived the mathematical model from the chemical reactions and the predicted pattern by their model has a good agreement with those experimental results. Also until recently, much research has been studied on the Turing patterns [18–20]. The main purpose of this article is to develop a fast and computationally efficient finite difference method for the Turing pattern on curved surfaces in the three-dimensional space. We solve the resulting discrete equations on a narrow band domain. We use an interpolation using the closest point method [21–23] for the domain boundary cells. We present numerical results of the zebra patterns generated by the proposed numerical method.

The layout of this paper is as follows. In Section 2, we describe the reaction–diffusion model on a narrow band domain. In Section 3, we provide the numerical solution algorithm. We present the numerical results in Section 4. In Section 5, conclusions are drawn.

2. The Lengyel–Epstein model on a narrow band domain

We consider the following reaction–diffusion equation [15] on a smooth closed surface $\mathcal{S}$ in $\mathbb{R}^3$:

$$\frac{\partial u}{\partial t} = D_u \Delta_\mathcal{S} u + f(u, v) = D_u \Delta_\mathcal{S} u + k_1 \left(v - \frac{uv}{1 + v^2} \right), \tag{1}$$

$$\frac{\partial v}{\partial t} = D_v \Delta_\mathcal{S} v + g(u, v) = D_v \Delta_\mathcal{S} v + k_2 - v - \frac{4uv}{1 + v^2}, \tag{2}$$

where $u(\mathbf{x}, t)$ and $v(\mathbf{x}, t)$ are concentrations of an inhibitor and an activator at position $\mathbf{x} \in \mathcal{S}$ and time t, respectively. Here, D_u and D_v are the diffusion coefficients, and k_1 and k_2 are positive constants related to the feed concentrations. Also, $\Delta_\mathcal{S}$ denotes the Laplace–Beltrami operator [24–27]. In this study, we represent a given smooth surface $\mathcal{S}$ using the signed distance function $\phi : \mathbb{R}^3 \to \mathbb{R}$. In other words, $\mathcal{S} = \{\mathbf{x} \in \mathbb{R}^3 : \phi(\mathbf{x}) = 0\}$ with $\phi < 0$ inside of $\mathcal{S}$ and $\phi > 0$ outside of $\mathcal{S}$. The tangential gradient of u on $\mathcal{S}$ is defined as $\nabla_\mathcal{S} u(\mathbf{x}, t) = \mathbf{P}(\mathbf{x}) \nabla u(\mathbf{x}, t)$, where $\mathbf{P} = \mathbf{I} - \nabla\phi \nabla\phi^T$ is a projection operator on the tangent space. Here, $\mathbf{I}$ is the identity matrix [28]. Then, the Laplace–Beltrami operator is defined as $\Delta_\mathcal{S} u = \nabla_\mathcal{S} \cdot \nabla_\mathcal{S} u = (\mathbf{P}\nabla) \cdot (\mathbf{P}\nabla u) = \nabla \cdot (\mathbf{P}\nabla u)$. Next, we define a δ-neighborhood band of S as $\Omega_\delta = \{\mathbf{y} | \mathbf{x} \in S, \mathbf{y} = \mathbf{x} + \theta \mathbf{n}(\mathbf{x}) \text{ for } |\theta| < \delta\}$, where $\mathbf{n}(\mathbf{x})$ is a unit normal vector at $\mathbf{x} \in S$. Fig. 1(a) shows the schematic illustration of the surface S, the narrow band domain Ω_δ, and the boundary $\partial\Omega_\delta$ of the narrow band domain Ω_δ. Let $\text{cp}(\mathbf{x})$ be a point in the surface S which is closest to $\mathbf{x}$ [24]. Fig. 1(b) shows the closest points $\text{cp}(\mathbf{x}_1)$ and $\text{cp}(\mathbf{x}_2)$ for boundary points $\mathbf{x}_1$ and $\mathbf{x}_2$ on $\partial\Omega_\delta$. Then, the boundary condition is defined as

$$u(\mathbf{x}, t) = u(\text{cp}(\mathbf{x}), t) \quad \text{and} \quad v(\mathbf{x}, t) = v(\text{cp}(\mathbf{x}), t) \quad \text{on } \partial\Omega_\delta. \tag{3}$$

If δ is small enough, then the temporal evolution of Eqs. (1) and (2) with the boundary condition (3) results in u and v which are constant in the direction normal to the surface. Therefore, we can replace the surface Laplacian operator Δ_s by the standard Laplacian operator Δ in the narrow band domain Ω_δ, i.e.,

$$\frac{\partial u}{\partial t} = D_u \Delta u + k_1 \left(v - \frac{uv}{1+v^2} \right),$$ (4)

$$\frac{\partial v}{\partial t} = D_v \Delta v + k_2 - v - \frac{4uv}{1+v^2}.$$ (5)

3. Numerical solution

We present a numerical algorithm for the Lengyel–Epstein model on the narrow band domain, Ω_δ. We discretize the reaction–diffusion equation in a three-dimensional domain $\Omega = (a,b) \times (c,d) \times (e,f)$ embedding Ω_δ. Let N_x, N_y, and N_z be positive integers, $h = (b-a)/N_x = (d-c)/N_y = (f-e)/N_z$ be the uniform mesh size, and $\Omega^h = \{\mathbf{x}_{ijk} = (x_i, y_j, z_k) = (a + hi, c + hj, e + hk)|0 \le i \le N_x, 0 \le j \le N_y, 0 \le k \le N_z\}$ be the discrete domain. Let u_{ijk}^n and v_{ijk}^n be approximations of $u(x_i, y_j, z_k, n\Delta t)$ and $v(x_i, y_j, z_k, n\Delta t)$, where $\Delta t = T/N_t$ is the time step, T is the final time, and N_t is the total number of time steps.

We adopt the numerical scheme used in the fast and accurate numerical method for motion by mean curvature of curves on a surface in three-dimensional space using the Allen–Cahn equation [23]. For a given smooth surface S, we define $\phi : \mathbb{R}^3 \to \mathbb{R}$ as the signed distance function to S so that $S = \{\mathbf{x} \in \mathbb{R}^3|\phi(\mathbf{x}) = 0\}$ with $\phi < 0$ inside S and $\phi > 0$ outside S. Let $\Omega_\delta^h = \{\mathbf{x}_{ijk}| |\phi_{ijk}| < \delta\}$ be the discrete narrow band domain. We take $\delta \ge \sqrt{3}h$ since Ω_δ^h must contain the interpolation stencil for the closest points of the domain boundary points. We define a discrete L^2-norm on Ω_δ^h as $\|\phi\|_{L^2(\Omega_\delta^h)} = \sqrt{\frac{1}{\#\Omega_\delta^h} \sum_{\mathbf{x}_{ijk} \in \Omega_\delta^h} \phi_{ijk}^2}$, where $\#\Omega_\delta^h$ is the cardinality of the set Ω_δ^h. Let us define the domain boundary points as $\partial\Omega_\delta^h = \{(x_i, y_j, z_k)|I_{ijk}|\nabla_h I_{ijk}| \ne 0\}$, where $\nabla_h I_{ijk} = (I_{i+1,jk} - I_{i-1,jk}, I_{i,j+1,k} - I_{i,j-1,k}, I_{ij,k+1} - I_{ij,k-1})/(2h)$. Here, $I_{ijk} = 0$ if $(x_i, y_j, z_k) \in \Omega_\delta^h$; otherwise $I_{ijk} = 1$. We consider the discretization of the reaction–diffusion system (4) and (5) using explicit scheme,

$$\frac{u_{ijk}^{n+1} - u_{ijk}^n}{\Delta t} = D_u \Delta_h u_{ijk}^n + k_1 \left(v_{ijk}^n - \frac{u_{ijk}^n v_{ijk}^n}{1 + (v_{ijk}^n)^2} \right),$$ (6)

$$\frac{v_{ijk}^{n+1} - v_{ijk}^n}{\Delta t} = D_v \Delta_h v_{ijk}^n + k_2 - v_{ijk}^n - \frac{4u_{ijk}^n v_{ijk}^n}{1 + (v_{ijk}^n)^2},$$ (7)

with the boundary condition on $\partial\Omega_\delta^h : u_{ijk}^n = u^n(\text{cp}(\mathbf{x}_{ijk}))$ and $v_{ijk}^n = v^n(\text{cp}(\mathbf{x}_{ijk}))$. Here, the discretization of second spatial derivative is given by $\Delta_h u_{ijk} = \frac{1}{h^2}(u_{i+1,jk} + u_{i-1,jk} + u_{i,j+1,k} + u_{i,j-1,k} + u_{ij,k+1} + u_{ij,k-1} - 6u_{ijk})$. The other one $\Delta_h v_{ijk}$ is similarly defined. We define the numerical closest point of the boundary point $\mathbf{x}_{ijk}$ to the surface S as

$$\text{cp}(\mathbf{x}_{ijk}) = \mathbf{x}_{ijk} - \frac{\nabla_h|\phi_{ijk}|}{|\nabla_h|\phi_{ijk}||}|\phi_{ijk}|.$$ (8)

If the closest point $\text{cp}(\mathbf{x}_{ijk})$ is not lying on a given computational grid, we obtain $u^n(\text{cp}(\mathbf{x}_{ijk}))$ and $v^n(\text{cp}(\mathbf{x}_{ijk}))$ by using the trilinear interpolation. For the fast computation, we tabulated the interpolation stencil and three fractions for each boundary point before starting time iterations.

4. Numerical experiments

4.1. Linear stability analysis

In this section, we study the linear stability analysis for Eqs. (4) and (5). We seek a solution of the form,

$$u(x, y, t) = \bar{u} + \alpha_{m_1,m_2}(t) \cos\left(\frac{2\pi m_1 x}{L_x}\right) \cos\left(\frac{2\pi m_2 y}{L_y}\right),$$ (9)

$$v(x, y, t) = \bar{v} + \beta_{m_1,m_2}(t) \cos\left(\frac{2\pi m_1 x}{L_x}\right) \cos\left(\frac{2\pi m_2 y}{L_y}\right),$$ (10)

where $\Omega = (0, L_x) \times (0, L_y)$ and $f(\bar{u}, \bar{v}) = g(\bar{u}, \bar{v}) = 0$. Substituting Eqs. (9) and (10) into the linearized equations of Eqs. (4) and (5) yields

$$\frac{d}{dt}\begin{pmatrix} \alpha_{m_1,m_2}(t) \\ \beta_{m_1,m_2}(t) \end{pmatrix} = A\begin{pmatrix} \alpha_{m_1,m_2}(t) \\ \beta_{m_1,m_2}(t) \end{pmatrix} = \begin{pmatrix} a & b \\ c & d \end{pmatrix}\begin{pmatrix} \alpha_{m_1,m_2}(t) \\ \beta_{m_1,m_2}(t) \end{pmatrix},$$ (11)
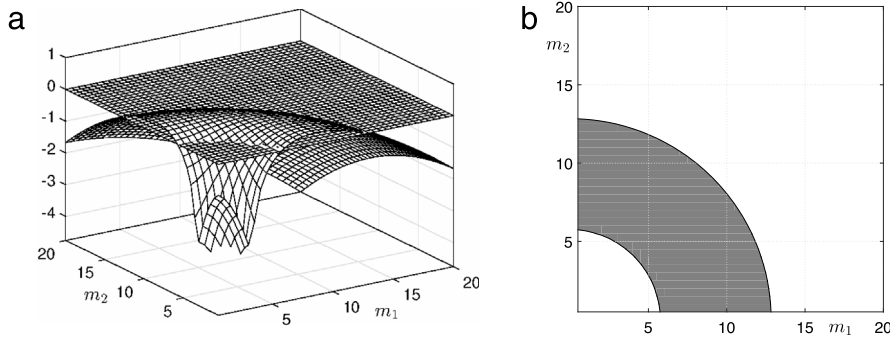
Fig. 2. (a) Mesh plot and (b) filled contour plot of $\max(Re(\lambda_1),\ Re(\lambda_2))$. Shaded area is the positive value of $\max(Re(\lambda_1),\ Re(\lambda_2))$.

where A is a 2×2 matrix whose components are given as

$$a = -D_u \left[\left(\frac{2\pi m_1}{L_x} \right)^2 + \left(\frac{2\pi m_2}{L_y} \right)^2 \right] - \frac{k_1 \bar{v}}{1 + \bar{v}^2}, \qquad (12)$$

$$b = k_1 \left[1 - \frac{\bar{u}(1 - \bar{v}^2)}{(1 + \bar{v}^2)^2} \right],$$

$$c = -\frac{4\bar{v}}{1 + \bar{v}^2}, \qquad (13)$$

$$d = -D_v \left[\left(\frac{2\pi m_1}{L_x} \right)^2 + \left(\frac{2\pi m_2}{L_y} \right)^2 \right] - 1 - \frac{4\bar{u}(1 - \bar{v}^2)}{(1 + \bar{v}^2)^2}.$$

Fig. 2(a) and (b) show the mesh plot and the contour plot of $\max(Re(\lambda_1),\ Re(\lambda_2))$, respectively, where λ_1 and λ_2 are the eigenvalues of the matrix A. For a better visualization, we put the zero plane together. Here, we used the parameters: $D_u = 1$, $D_v = 0.02$, $k_1 = 9$, $k_2 = 11$, $\bar{u} = 1 + 0.04 k_2^2$, $\bar{v} = 0.2 k_2$, $L_x = 10$, and $L_y = 10$.

4.2. Pattern on two-dimensional rectangular domain

We first numerically solve Eqs. (1) and (2) on a two-dimensional rectangular domain $\Omega = [0, 10] \times [0, 10]$ using $D_u = 1$, $k_2 = 11$, a mesh grid 101×101, $h = 0.1$, and $\Delta t = 0.1 h^2$. Here, periodic boundary conditions in each direction are used. Initial conditions for u and v are $u(x, y, 0) = \bar{u} + 0.1\ \text{rand}(x, y)$, $v(x, y, 0) = \bar{v} + 0.1\ \text{rand}(x, y)$, where $\bar{u} = 1 + 0.04 k_2^2$, $\bar{v} = 0.2 k_2$, and $\text{rand}(x, y)$ is a random number between -1 and 1.

Fig. 3(a) and (b) show the temporal evolutions of the activator concentration (v) when we use $D_v = 0.04$, $k_1 = 7$ and $D_v = 0.02$, $k_1 = 9$, respectively. The times are shown below each column. We can observe spots and stripes depending on the parameters as shown in [29]. Note that Othmer et al. [29] showed more patterns observed in animal skin, including spots, stripes, reticulated stripes, and inverted spots.

4.3. Parameter study on pattern formation on spherical surface

Next, we investigate the effect of parameters D_v and k_1 on the pattern dynamics on the surface of a sphere with radius 4.5. The spherical surface is represented by the zero level set of the signed distance function

$$\phi(x, y, z) = \sqrt{(x - 5)^2 + (y - 5)^2 + (z - 5)^2} - 4.5.$$

For the numerical simulation, we use the same parameter values for k_1, k_2, D_u, and D_v as in [29]. The initial conditions are taken to be

$$u(x, y, z, 0) = 1 + 0.04 k_2^2 + 0.1\ \text{rand}(x, y, z), \qquad (14)$$

$$v(x, y, z, 0) = 0.2 k_2 + 0.1\ \text{rand}(x, y, z), \qquad (15)$$

where $\text{rand}(x, y, z)$ is a random number between -1 and 1. The parameters used are $D_u = 1$, $k_2 = 11$, $h = 0.1$, $\delta = 1.1\sqrt{3}h$, $\Delta t = 0.1 h^2$, and $T = 1000$ on the computational domain $\Omega = [0, 10]^3$. Fig. 4 represents numerical solutions of activator v by Eqs. (6) and (7) with respect to D_v and k_1. Depending on the parameter sets (D_v, k_1), we obtain the numerical results such as spots, stripes, and mixtures of spots and stripes. In the upper and right sides in Fig. 4, Turing instability does not occur.
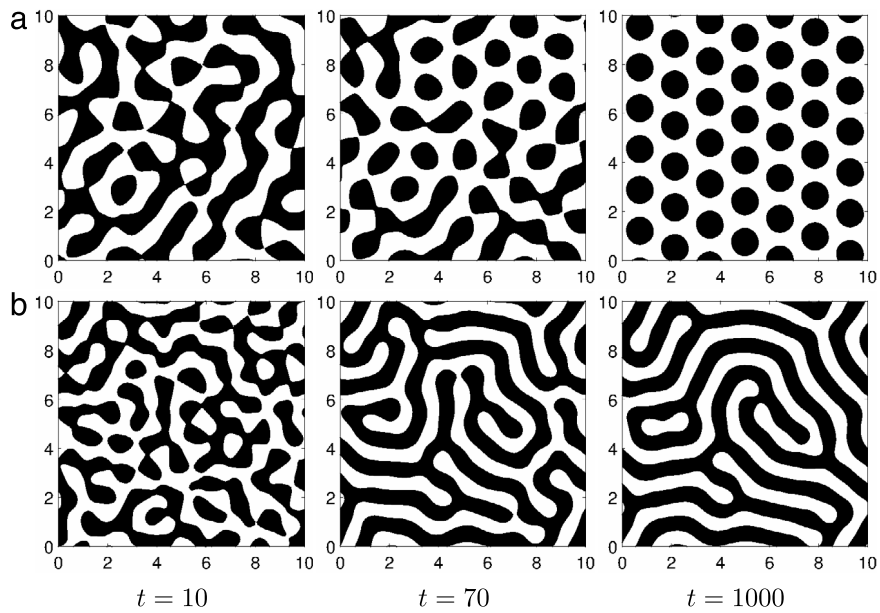
Fig. 3. Temporal evolution of activator concentration with $D_u = 1$ and $k_2 = 11$ on two-dimensional domain $\Omega = [0, 10] \times [0, 10]$. Here, (a) $D_v = 0.04$, $k_1 = 7$ and (b) $D_v = 0.02$, $k_1 = 9$ are used.
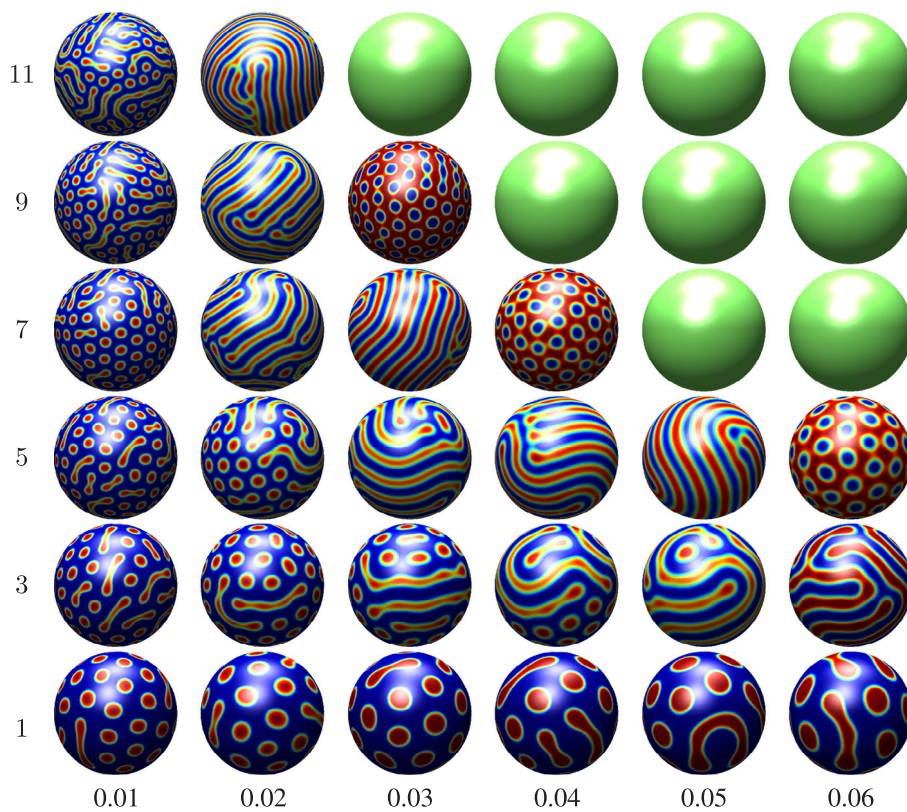

Fig. 4. Overview of pattern formation on surface of sphere corresponding to concentration of activator (v) at different values of D_v (horizontal axis) and k_1 (vertical axis).
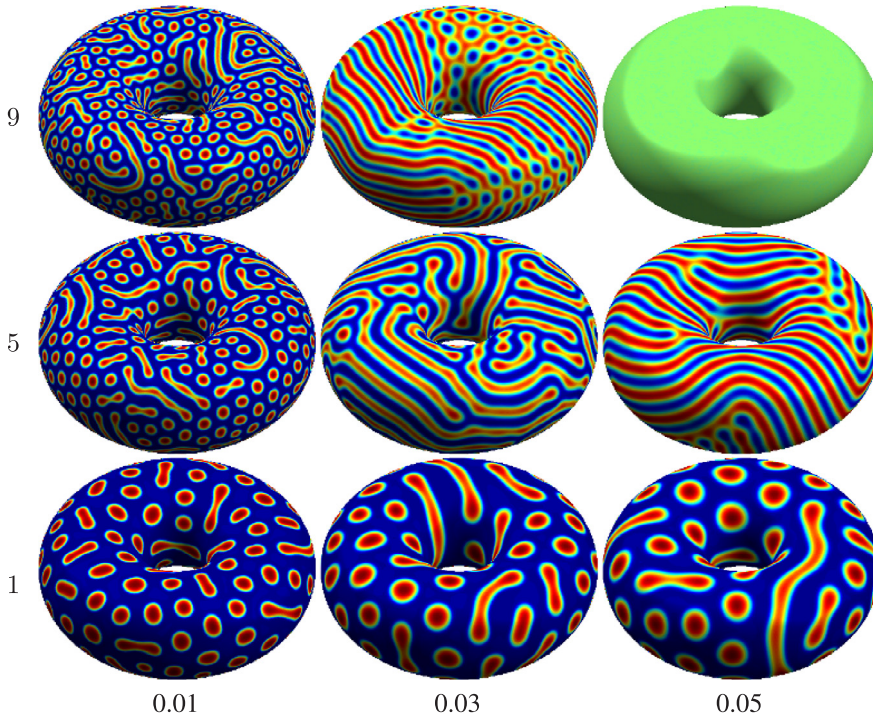
Fig. 5. Pattern formation on the torus surface with the different values of D_v (horizontal axis) and k_1(vertical axis).

4.4. Parameter study on pattern formation on torus surface

As in the previous section, we study the pattern formation with the various values of the parameters (D_v and k_1) on the torus surface with major radius 5.5 and minor radius 3.5. The torus surface is represented by the zero level set of a signed distance function

$$\phi(x, y, z) = \sqrt{(\sqrt{x^2 + y^2} - 5.5)^2 + z^2} - 3.5.$$

For the numerical simulation, we use the same parameter values and initial conditions as in the previous section. The parameters used are $D_u = 1$, $k_2 = 11$, $h = 0.1$, $\delta = 1.1\sqrt{3}h$, $\Delta t = 0.1h^2$, and $T = 1000$ on the computational domain $\Omega = [0, 10]^3$. Fig. 5 represents numerical solutions of activator v. We obtain the similar numerical results as in the previous section such as spots, stripes, and mixtures of spots and stripes from each cases (D_v, k_1). In the case of $k_1 = 9$ and $D_v = 0.05$, Turing instability does not occur.

4.5. Stripe patterns on zebra surface

To solve the reaction–diffusion system (6) and (7) on the surface of a zebra surface, we need a narrow band domain for the zebra surface. First, we obtain a 3ds file format for a three-dimensional zebra model which is available in [30]. Next, we extract the geometry information such as vertices and triangles by using Autodesk®3DS MAX®. Fig. 6(a) shows the vertices of the zebra. However, some regions do not contain sufficient points for constructing a smooth surface. We add more points as shown in Fig. 6(b).

The procedure of adding points is as follows: Let *tol* be a tolerance which is a maximum size of the sides of the triangles. Loop over the triangles recursively until all the sides of the triangles are less than the given tolerance. For example, take a triangle consisting of three vertices P_1, P_2, P_3 and divide the triangle and add mid points until the maximum size of the sides is less than the given tolerance, see Fig. 7(a)–(d).

Now, we need to get the surface of zebra as the zero level set of a scalar function from the scattered data points. In this step, we apply an image segmentation technique which was proposed by Li and Kim [31]. For the segmentation, the governing equation is given as

$$\frac{\partial \phi(\mathbf{x}, t)}{\partial t} = g(\mathbf{x}) \left(-\frac{F'(\phi(\mathbf{x}, t))}{\epsilon^2} + \Delta \phi(\mathbf{x}, t) + \beta F(\phi(\mathbf{x}, t)) \right), \tag{16}$$

where $g(\mathbf{x})$ is the unsigned distance function constructed from the unorganized data set of zebra, ϕ is a phase-field function, which is close to 1 and -1 in the inside and outside domain of the reconstructed zebra. Fig. 8(a) represents the zero isosurface
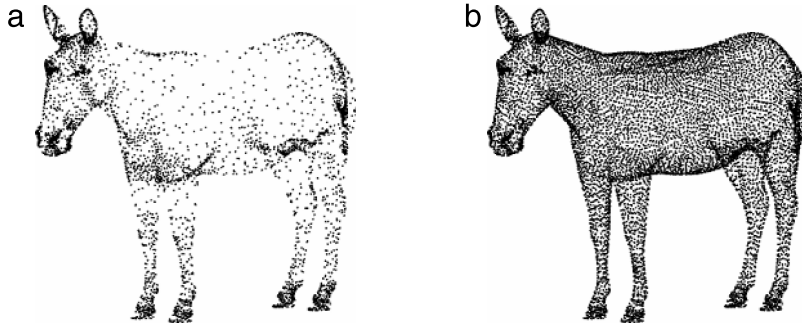
Fig. 6. (a) Given unorganized data set of zebra and (b) enriched data set.
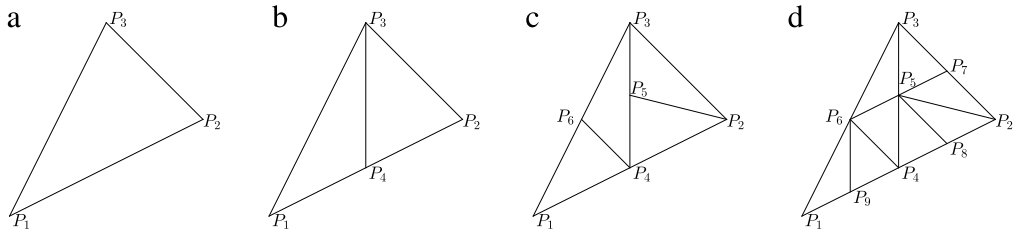

Fig. 7. Recursively supplement points into polygon: (a) initial polygon, (b) first iteration, (c) second iteration, and (d) third iteration.
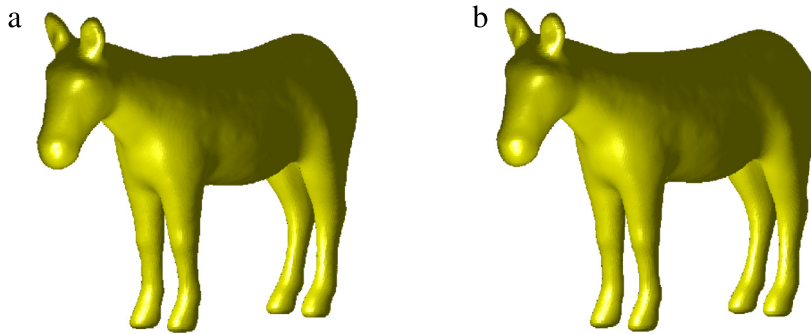

Fig. 8. Zero isosurface (a) before and (b) after reinitialization step.

of the segmented image using Eq. (16) with $\epsilon = 0.0225$ and $\lambda = 500$. Here, a $64 \times 256 \times 192$ mesh grid on the domain $\Omega = (0, 1) \times (0, 4) \times (0, 3)$ and $\Delta t = 0.001$ are used.

Finally, we construct the signed distance function from the unsigned distance function which is obtained in the previous step, since $|\nabla \phi|$ is not one in the neighborhood of $\mathcal{S}$, i.e., $\phi = 0$. To obtain the signed distance function (Fig. 8(b)), we apply the following equation:

$$\phi_t = S_\delta(\phi^0)(1 - \sqrt{\phi_x^2 + \phi_y^2 + \phi_z^2}), \tag{17}$$

where $\phi_0 = \phi(\mathbf{x}, 0)$ and $S_\delta(\phi^0) = \phi^0/\sqrt{(\phi^0)^2 + \delta^2}$ is a smoothed sign function [32].

Depending on varying parameters, different kinds of stripe patterns on a given zebra surface are generated. To investigate this, we take the initial conditions (14) and (15). The other parameters used are as follows: $D_u = 1, k_2 = 11, h = 10/64$, $\delta = 1.1\sqrt{3}h, \Delta t = 0.1h^2, T = 2441.4$, and $\Omega = [0, 84h] \times [0, 276h] \times [0, 212h]$. For k_1 and D_v, we use the three different values as $(k_1, D_v) = (11, 0.02), (k_1, D_v) = (5, 0.04)$, and $(k_1, D_v) = (3, 0.06)$. Here, for the chosen parameters, we may refer to [11].

Fig. 9 represents the temporal evolution of morphological patterns of activator v on the zebra surface with different values of (k_1, D_v). The computational times are listed below each row. In this figure, we plot the pattern with a local grayscale corresponds to white and black with maximum and minimum concentration of activator v. As k_2 decreases and D_v increases, the thickness of the stripes are larger.

Fig. 9. Pattern formation process of the Lengyel–Epstein model on a zebra surface with $k_1 = 11$ and $D_u = 1$ at $t = 1000\Delta t$, $10\,000\Delta t$, $100\,000\Delta t$, and $100\,000\Delta t$. Here, the other parameters are used (a) $k_2 = 11$, $D_v = 0.02$, (b) $k_2 = 5$, $D_v = 0.04$, and (c) $k_2 = 3$, $D_v = 0.06$, respectively.

4.6. Extension of a non-local coupled Lengyel–Esptein model

Next, we consider a non-local coupling, i.e., the following integro-differential equations as

$$\frac{\partial u(\mathbf{x}, t)}{\partial t} = f(u(\mathbf{x}, t), v(\mathbf{x}, t)) + D_u \int_{\Omega} \sigma(\mathbf{x}, \mathbf{x}')u(\mathbf{x}', t)\mathrm{d}\mathbf{x}', \tag{18}$$

$$\frac{\partial v(\mathbf{x}, t)}{\partial t} = g(u(\mathbf{x}, t), v(\mathbf{x}, t)) + D_v \int_{\Omega} \sigma(\mathbf{x}, \mathbf{x}')v(\mathbf{x}', t)\mathrm{d}\mathbf{x}', \tag{19}$$

where $\sigma(\mathbf{x}, \mathbf{x}')$ is a non-local interaction kernel. Based on the activator–inhibitor system with power-law coupling [9], we extend a non-local coupled Lengyel–Epstein model to a three-dimensional space and discretize this model by using the explicit scheme as follows:

$$\frac{u_{ijk}^{n+1} - u_{ijk}^n}{\Delta t} = k_1 \left(v_{ijk}^n - \frac{u_{ijk}^n v_{ijk}^n}{1 + (v_{ijk}^n)^2} \right) + \frac{6D_u}{h^2 \kappa_{ijk}(\alpha)} \sum_{(p,q,r) \in \Omega_{ijk}^m} \frac{u_{i+p,j+q,k+r}^n - u_{ijk}^n}{(p^2 + q^2 + r^2)^{\alpha/2}}, \tag{20}$$
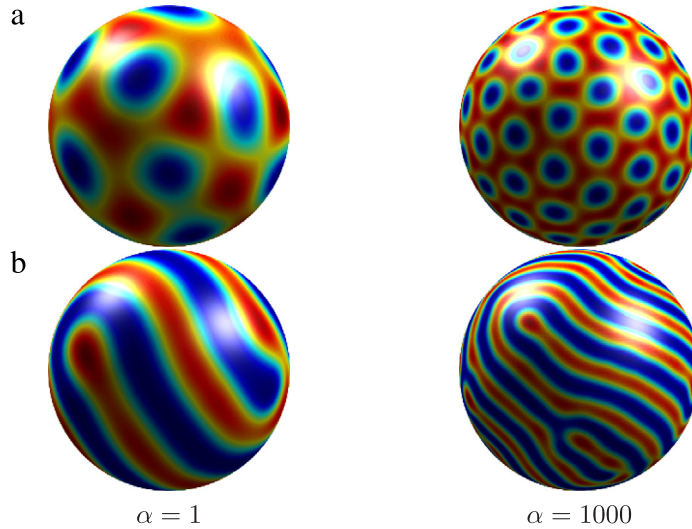
a

b

$\alpha = 1$ $\alpha = 1000$

Fig. 10. Patterns of the activator in a non-local coupled Lengyel–Epstein model with respect to α on the surface of sphere. Here, $D_u = 1$, $k_1 = 9$, $k_2 = 11$, and (a) $D_v = 0.03$; (b) $D_v = 0.02$ are used.

$$\frac{v_{ijk}^{n+1} - v_{ijk}^n}{\Delta t} = k_2 - v_{ijk}^n - \frac{4 u_{ijk}^n v_{ijk}^n}{1 + (v_{ijk}^n)^2} + \frac{6 D_v}{h^2 \kappa_{ijk}(\alpha)} \sum_{(p,q,r) \in \Omega_{ijk}^m} \frac{v_{i+p,j+q,k+r}^n - v_{ijk}^n}{(p^2 + q^2 + r^2)^{\alpha/2}}. \tag{21}$$

Here, $\Omega_{ijk}^m = \{(p, q, r) | -m \le p, q, r \le m, \; \mathbf{x}_{i+p,j+q,k+r} \in \Omega_\delta^h, \; |p| + |q| + |r| \ne 0\}$ and $\kappa_{ijk}(\alpha) = \sum_{(p,q,r) \in \Omega_{ijk}^m} (p^2 + q^2 + r^2)^{-0.5\alpha}$.

Now, we perform several numerical tests with the non-local coupled Lengyel–Epstein model to show effect of an exponent α, that is, non-local factor. First, we perform a numerical test on the surface of sphere with $\alpha = 1$ and $\alpha = 1000$. For this test, we use the following spherical surface which is represented by the zero level set of the signed distance function:

$$\phi(x, y, z) = \sqrt{(x - 5)^2 + (y - 5)^2 + (z - 5)^2} - 3.5$$

on the computational domain $\Omega = (0, 10)^3$. The initial conditions are taken to Eqs. (14) and (15). As a representative example, we use two different values $D_v = 0.03$ and $D_v = 0.02$. The other parameters used are as $D_u = 1$, $k_1 = 9$, $k_2 = 11$, $h = 0.1$, and $N_x = N_y = N_z = 101$, $\Delta t = 0.1 h^2$, and $\delta = 1.1\sqrt{3}h$, $m = 2$ in all tests. Fig. 10 shows the numerical solutions at $T = 1\,000\,000 \Delta t$. Depending on the values of D_v, we see the dotted and lamella patterns. As the value of α decreases, the diffusion term has more global effect. Also, the spatial–temporal patterns appear larger one.

As second example, we perform a numerical test on the surface of torus, which is represented by the following the signed distance function as

$$\phi(x, y, z) = \sqrt{\left(\sqrt{x^2 + y^2} - 3 \right)^2 + z^2} - 1.5.$$

We use the same values as the previous test for the other parameters. Fig. 11 represents the numerical results at $T = 1\,000\,000 \Delta t$ when $\alpha = 1$ and $\alpha = 1000$. Like the previous test, we see that the temporal patterns get smaller as α increases.

Finally, we apply the non-local coupled Lengyel–Esptein model on the surface of zebra. In this test, we use the same value which is used in Fig. 9. Fig. 12 shows the numerical results at $T = 1\,000\,000 \Delta t$ with $\alpha = 1$ and $\alpha = 1000$. We can observe the non-local factor α effect on the zebra surface.

5. Conclusions

In this article, we numerically studied the zebra skin pattern formation on the surface of a zebra model in three-dimensional space using a two-component activator–inhibitor system of reaction–diffusion equations. We discretized the governing equations using a finite difference method and solved the resulting system on a discrete narrow band domain containing the zebra skin. For the domain boundary cells, we used an interpolation using the closest point method. We presented numerical results of the zebra patterns generated by the model. Depending on parameter sets, we had different spatial pattern formations such as spots, stripes, and mixture of spots and stripes as shown in two-dimensional rectangular space. Also, we can see this results on zebra surface, which is more complex than sphere, as well as sphere. From the numerical tests, we knew that the condition that distinguish between stripe or spots is determined by D_v in reaction–diffusion systems and k_1 plays a role in decision of the wavelength of pattern. Especially, we obtained the similar numerical pattern on given zebra surface to the real one. In future work, we will investigate space-dependent variable model coefficient to simulate the realistic zebra pattern formations.
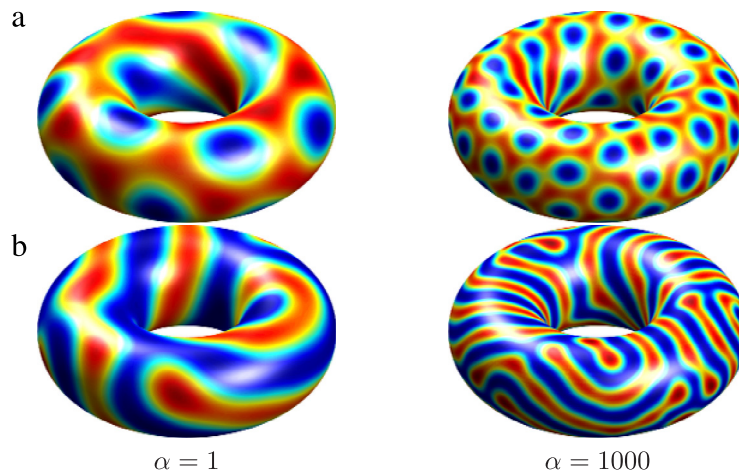
Fig. 11. Patterns of the activator in a non-local coupled Lengyel–Epstein model with respect to α on the surface of torus. Here, $D_u = 1$, $k_1 = 9$, $k_2 = 11$, and (a) $D_v = 0.03$; (b) $D_v = 0.02$ are used.
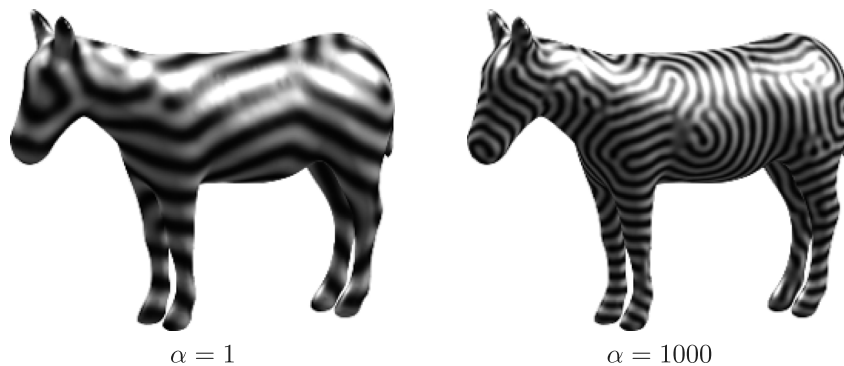

Fig. 12. Patterns of the activator in a non-local coupled Lengyel–Epstein model with respect to α. Here, $D_u = 1$, $k_1 = 9$, $k_2 = 11$, $D_v = 0.02$ are used.

Acknowledgments

References

[1] C.P. Gravan, R. Lahoz-Beltra, Evolving morphogenetic fields in the zebra skin pattern based on Turing's morphogen hypothesis, Int. J. Appl. Math. Comput. Sci. 14 (2004) 351–362.
[2] B. Ermentrout, Stripes or spots? Nonlinear effects in bifurcation of reaction-diffusion equations on the square, Int. Proc. R. Soc. A 434 (1991) 413–417.
[3] M.J. Lyons, L.G. Harrison, Stripe selection: An intrinsic property of some pattern-forming models with nonlinear dynamics, Dev. Dyn. 195 (1992) 201–215.
[4] M.C. Mackey, P.K. Maini, What has mathematics done for biology? Bull. Math. Biol. 77 (2015) 735–738.
[5] A.M. Turing, The chemical basis of morphogenesis, Philos. Trans. R. Soc. B 237 (1952) 37–72.
[6] J.D. Murray, A pre-pattern formation mechanism for animal coat markings, J. Theoret. Biol. 88 (1981) 161–199.
[7] D.A. Young, A local activator-inhibitor model of vertebrate skin patterns, Math. Biosci. 72 (1984) 51–58.
[8] R.A. Barrio, C. Varea, J.L. Aragón, P.K. Maini, A two-dimensional numerical study of spatial pattern formation in interacting Turing systems, Bull. Math. Biol. 61 (1999) 483–505.
[9] F.D.S. Silva, R.L. Viana, S.R. Lopes, Pattern formation and Turing instability in an activator-inhibitor system with power-law coupling, Physica A 419 (2015) 487–497.
[10] K.J. Painter, P.K. Maini, H.G. Othmer, Stripe formation in juvenile Pomacanthus explained by a generalized Turing mechanism with chemotaxis, Proc. Natl. Acad. Sci. 96 (1999) 5549–5554.
[11] J. Guiu-Souto, J. Carballido-Landeira, A.P. Munuzuri, Characterizing topological transitions in a Turing-pattern-forming reaction-diffusion system, Phys. Rev. E 85 (2012) 056205.
[12] V. Castets, E. Dulos, P.D. Kepper, Experimental evidence of a sustained standing Turing-type nonequilibrium chemical pattern, Phys. Rev. Lett. 64 (1990) 2953–2956.

[13] P. Kepper, V. Castets, E. Dulos, J. Boissonade, Turing-type chemical patterns in the chlorite-iodide-malonic acid reaction, Physica D 49 (1991) 161–169.
[14] Q. Ouyang, H.L. Swinney, Transition from a uniform state to hexagonal and striped turing patterns, Nature 352 (1991) 610–612.
[15] I. Lengyel, I.R. Epstein, Modeling of Turing structure in the Chlorite–Iodide–Malonic acid–Starch reaction system, Science 251 (1991) 650–652.
[16] I. Lengyel, I.R. Epstein, A chemical approach to designing Turing patterns in reaction-diffusion system, Proc. Natl. Acad. Sci. 89 (1992) 3977–3979.
[17] H. Shoji, T. Ohta, Computer simulations of three-dimensional Turing patterns in the Lengyel–Epstein model, Phys. Rev. E 91 (2015) 032913.
[18] Y. Cao, R. Erban, Stochastic Turing patterns: Analysis of compartment-based approaches, Bull. Math. Biol. 76 (2014) 3051–3069.
[19] D. Haile, Z. Xie, Long-time behavior and Turing instability induced by cross-diffusion in a three species food chain model with a Holling type-II functional response, Math. Biosci. 267 (2015) 134–148.
[20] R.D. Parshad, N. Kumari, A.R. Kasimov, H.A. Abderrahmane, Turing patterns and long-time behavior in a three-species food-chain model, Math. Biosci. 254 (2014) 83–102.
[21] C.B. Macdonald, J.R. Steven, Level set equations on surfaces via the closest point method, J. Sci. Comput. 35 (2008) 219–240.
[22] D. Jeong, J. Kim, Microphase separation patterns in diblock copolymers on curved surfaces using a nonlocal Cahn–Hilliard quation, Eur. Phys. J. E 38 (2015) 1–7.
[23] Y. Choi, D. Jeong, S. Lee, M. Yoo, J. Kim, Motion by mean curvature of curves on surfaces using the Allen–Cahn equation, Internat. J. Engrg. Sci. 97 (2015) 126–132.
[24] C.B. Macdonald, J. Brandman, S.J. Ruuth, Solving eigenvalue problems on curved surfaces using the closest point method, J. Comput. Phys. 230 (2011) 7944–7956.
[25] S. Angenent, S. Haker, A.R. Tannenbaum, R. Kikinis, On the Laplace–Beltrami operator and brain surface flattening, IEEE Trans. Med. Imaging 18 (1999) 700–711.
[26] R.G. Plaza, F. Sanchez-Garduno, P. Padilla, R.A. Barrio, P.K. Maini, The effect of growth and curvature on pattern formation, J. Dynam. Differential Equations 16 (2004) 1093–1121.
[27] G. Toole, M.K. Hurdal, Turing models of cortical folding on exponentially and logistically growing domains, Comput. Math. Appl. 66 (2013) 1627–1642.
[28] J.B. Greer, An improvement of a recent Eulerian method for solving PDEs on general geometries, J. Sci. Comput. 29 (2006) 321–352.
[29] H.G. Othmer, K. Painter, D. Umulis, C. Xue, The intersection of theory and application in Elucidating pattern formation in developmental biology, Math. Model. Nat. Phenom. 4 (2009) 3–82.
[30] G. Terragni, 2014. URL: http://open3dmodel.com/download/zebra-3d-model_3220.html.
[31] Y. Li, J. Kim, A fast and accurate numerical method for medical image segmentation, J. KSIAM 14 (2010) 201–210.
[32] M. Sussman, P. Smereka, S. Osher, A level set approach for computing solutions to incompressible two-phase flow, J. Comput. Phys. 114 (1994) 146–159.